I. HIGH-FREQUENCY TECHNIQUES FOR RCS PREDICTION OF PLATE GEOMETRIES

A. INTRODUCTION

Important research areas involving high-frequency scattering prediction techniques that have been discussed in previous reports include the development of techniques for modeling corner diffraction, nonprincipal-plane scattering, and scattering from coated conducting geometries [1, 2, 3, 4, 5, 6, 7, 8, 9]. The most recent reports have dealt mainly with the principal-plane radar cross section (RCS) prediction of a perfectly conducting rectangular plate coated on one side with an electrically thin ($t \ll \lambda$), lossy dielectric [3, 4, 5, 6, 7, 8, 9]. This is an important geometry to consider because its simplicity allows the isolation of individual scattering mechanisms while its generality enables its incorporation into more complex modeling geometries. In other words, the plate geometry allows one to develop and validate modeling techniques for higher-order mechanisms, such as multiple diffractions and multiply diffracted surface waves, with the eventual goal of being able to apply these techniques to general, coated conducting geometries.

This report presents and validates a Uniform Theory of Diffraction (UTD) model for the principal-plane RCS prediction of a coated conducting rectangular plate. The incorporation of higher-order multiple diffraction terms and of higher-order surface-wave terms is discussed. The necessity of including higher-order mechanisms is demonstrated. The model is validated by comparisons with experimental results, and its superiority over a simple physical optics (PO) model is demonstrated. Other models exist for the coated plate geometry [10, 11]; however, the model presented in this report incorporates higher-order terms which were not included in these earlier models. Specifically, the work by Knop and Cohn [10] is based upon a physical optics (PO) approach, which does not include edge ef-

fects. The model presented by Bhattacharyya and Tadon [11], although similar in approach to the method used in this report, includes only first- and second-order diffractions. The model presented here includes first-, second-, and third-order regular diffractions and second- and third-order surface-wave diffractions. These additional terms are crucial to obtaining accurate results.

The modeling of the scattered fields from coated conducting targets is a subject of interest both to those developing low-frequency modeling techniques and to those developing high-frequency techniques. The development of low-frequency techniques has been quite successful. Both the moment method (MM) and the finite-difference time-domain (FDTD) techniques can be used to accurately predict the RCS of a coated plate [12]. Because these techniques are low-frequency techniques, the size of the geometry that can easily be modeled is limited by computational time and memory requirements. Thus, it is important to develop high-frequency techniques, which are inherently more appropriate for electrically large structures.

The model developed in this report is based upon the UTD diffraction coefficients for an impedance wedge [13, 14]. The effects of the finite thickness lossy coating backed by a perfect conductor are included using the short-circuited transmission-line approximation. Although a simple model, it will be demonstrated that this model is accurate near and at normal incidence and sufficient for other angles. The model presented in this report is computationally fast and simple and increases in accuracy as the electrical size of the geometry increases and as the electrical thickness of the coating becomes smaller. These are desirable and expected properties of a high-frequency method.

Other work on high-frequency methods for modeling coated conducting geometries includes more sophisticated ways of dealing with problems of importance. For example, Herman and Volakis [15] have dealt extensively with the modeling of scatterers in overlapping transition regions using the Extended Spectral Ray Method (ESRM). Volakis and Senior [16] have investigated the scattering

by a metal-backed dielectric half plane using higher-order generalized impedance boundary conditions. Rojas and Chou [17] have also explored solutions to partially coated conducting geometries using generalized impedance boundary conditions. Finally, Bernard [18] developed a solution for the specific case of a conducting wedge covered by a dielectric material. Because all of this work focuses on specific problems inherent in developing high-frequency techniques for dealing with coated conductors, the results obtained are highly accurate for the problems of interest. The techniques are not inherently easy to apply to more general geometries. The goal of the research outlined in this report is to develop general models, for coated conducting geometries, that are easily implemented and computationally fast and accurate. Thus, the model outlined in this report uses a simple boundary condition, the impedance boundary condition, which is incorporated into the short-circuited transmission-line approximation, to model the effects of a finite-thickness coating backed by a perfect conductor. Also, a straightforward application of the UTD, based upon the coefficients for the impedance wedge, is applied. Future research will attempt to incorporate ideas from the aforementioned research into the general model.

B. THEORY AND RESULTS

1. UTD Plate Model

The UTD plate model consists of two parallel impedance wedges separated by a distance, w, equal to the plate width. The wedge geometry is shown in Fig. 1. To obtain the plate model illustrated in Fig. 2, the left and right wedge included angles are set to 0°, or the wedge parameter is set to $n = 2$. For the coated plate, the bottom face of each wedge is modeled as a perfect conductor with $\eta_2 = 0$. The top face of each wedge is modeled by an equivalent impedance appropriate for the coating. The plate is modeled two-dimensionally in the principal plane, and

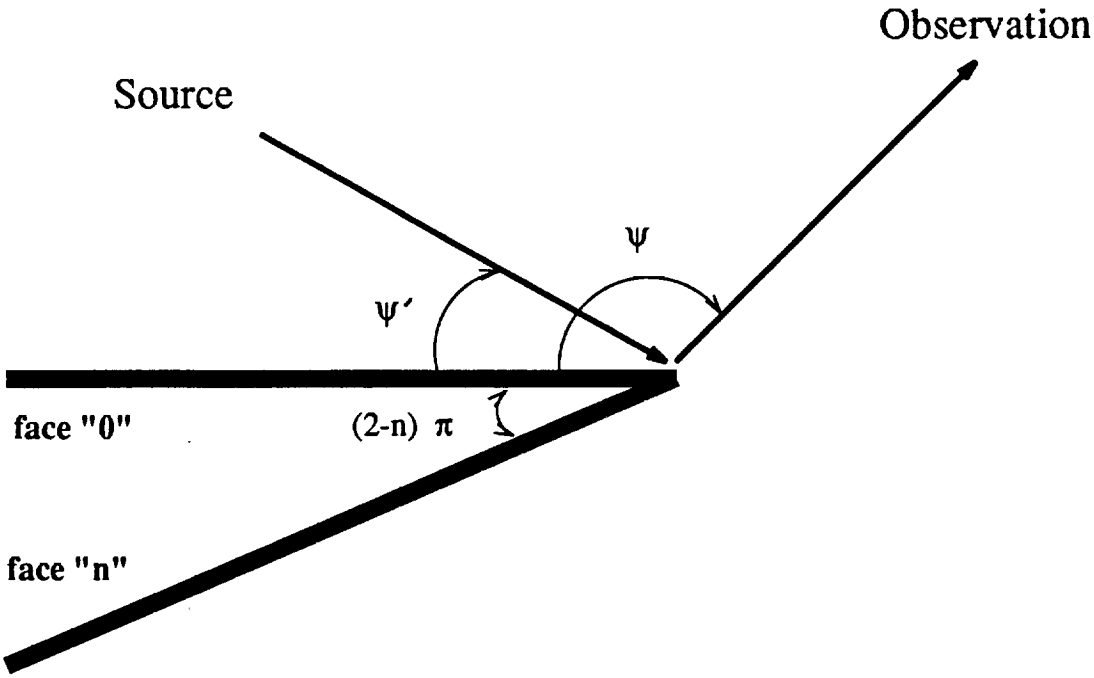

Figure 1: Impedance wedge geometry.

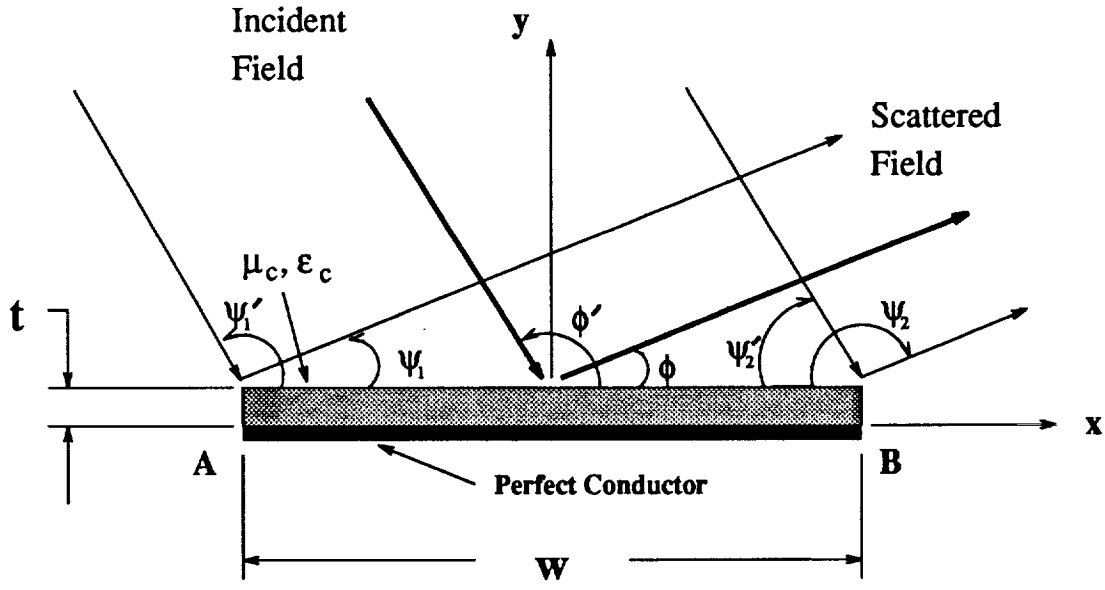

Figure 2: Geometry for principal-plane scattering from a strip/plate with a finite-thickness coating backed by a perfect conductor.

three-dimensional results are obtained using Ross's truncation approximation [19]:

$$\sigma_{3-D} = \frac{2L^2}{\lambda}\sigma_{2-D} \tag{1}$$

It is important that the impedance of the coating be modeled accurately, yet simply, so that the model remains computationally fast and easy to implement. For these reasons, the short-circuited transmission-line approximation is used to express the normalized equivalent impedance of the top face of each wedge as [8]:

$$\eta_0 = j\sqrt{\frac{\mu_c}{\epsilon_c}}\tan\left(2\pi\sqrt{\mu_c\epsilon_c}t\right) \tag{2}$$

where μ_c and ϵ_c are the relative permeability and permittivity, respectively, of the coating; and t is the thickness of the coating in free-space wavelengths. Both μ_c and ϵ_c can be complex numbers, so η_0 is usually a complex quantity.

A first-order model which accounts for diffractions from each of the wedges comprising the plate is not sufficient for accurate RCS prediction. As will be demonstrated, interactions between the wedges are crucial scattering mechanisms. The model of this work contains second- and third-order diffraction terms, in addition to first-order mechanisms. Also, second- and third-order surface-wave terms are included.

Higher-order diffraction terms are formulated by consecutively multiplying the appropriate diffraction coefficients by the phase and amplitude spreading factors. The diffraction coefficients used are the UTD coefficients derived by Tiberio, *et al.* [13], and further revised by Griesser and Balanis [14]. These were based upon Maliuzhinets' solution for the scattering by an impedance wedge [20]. The particular coefficients and methods of calculation were explicitly detailed in a previous report [8] and, therefore, will not be repeated here. For reference, the notation for the specific coefficients, their particular use, and the number of the equation in [8] that gives the expression for the coefficient are given in the following table:

Table of Coefficients		
Usage	Notation	Equation Reference in [8]
1st-order Diffractions (Plane-wave Incidence, Far-field Observation)	$D_{ff}(\psi', \psi, \theta_0, \theta_2 = 0, n = 2)$	Eq. (4) with Fresnel Functions set to unity ($F[x] = 1$)
Higher-order Diffractions (Plane-wave Incidence, Observation at a Finite Distance)	$D_{pwfd}(\rho', \psi', \psi, \theta_0, \theta_2 = 0, n = 2)$	Eq. (4)
Higher-order Diffractions (Cylindrical-wave Incidence, Far-field Observation)	$D_{cwff}(\rho, \psi', \psi, \theta_0, \theta_2 = 0, n = 2)$	Eq. (4) with ρ substituted for ρ' and ψ' and ψ switched
Surface Wave Field	$U_{sw}(\rho, \psi', \psi, \theta_0, n = 2)$	Eq. (19)
Surface Wave Transition Field	$U_{swtr}(\rho, \psi', \psi, \theta_0, n = 2)$	Eq. (21)

The angles of incidence and observation with respect to the wedge of interest are ψ' and ψ, respectively. In [8], these were designated as ϕ' and ϕ. The distance from the source to the point of diffraction is ρ' while ρ is the diffraction distance. The Brewster angles, θ_0 and θ_n, of the top and bottom faces of the wedge are, respectively, given by Eqs. (2) and (3) of [8]. The wedge parameter is n, and it is equal to 2 for a half plane.

The second-order diffracted fields actually consist of four mechanisms; two emanating from each edge of the plate. Fig. 3 illustrates the mechanisms for the right side of the plate. The field incident on the left side of the plate diffracts along both the top and bottom of the plate. Each of these diffracted fields then diffracts from the right side of the plate. Analogous mechanisms exist for the left side of the plate for a total of four second-order mechanisms. The total second-order diffracted field is:

$$\mathbf{E_{2nd}} = \mathbf{E_i} \frac{e^{-jk\rho}}{\sqrt{k\rho}} \frac{e^{-jkw}\sqrt{k}}{2\sqrt{w}} \left\{ e^{j\frac{kw}{2}(\cos\phi' - \cos\phi)} \right.$$

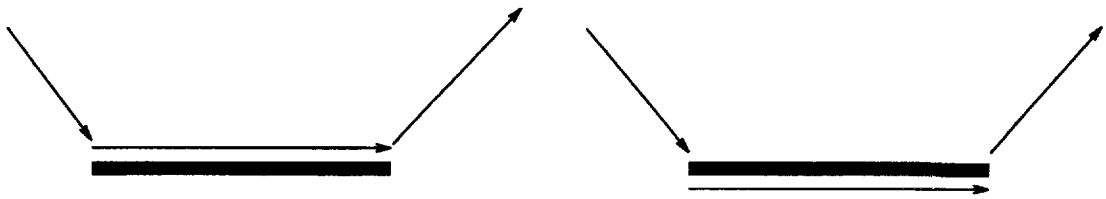

Figure 3: Second-order scattering terms emanating from the right edge of the plate.

$$
\begin{aligned}
&\times \; [D_{pwfd}(w, \psi_2', 0°, \theta_0, \theta_2 = 0, n = 2) \\
&\times \; D_{cwff}(w, 0°, \psi_1, \theta_0, \theta_2 = 0, n = 2) \\
&+ \; D_{pwfd}(w, \psi_2', 360°, \theta_0, \theta_2 = 0, n = 2) \\
&\times \; D_{cwff}(w, 360°, \psi_1, \theta_0, \theta_2 = 0, n = 2)] \\
&+ \; e^{-j\frac{kw}{2}(\cos\phi' - \cos\phi)} \\
&\times \; [D_{pwfd}(w, \psi_1', 0°, \theta_0, \theta_2 = 0, n = 2) \\
&\times \; D_{cwff}(w, 0°, \psi_2, \theta_0, \theta_2 = 0, n = 2) \\
&+ \; D_{pwfd}(w, \psi_1', 360°, \theta_0, \theta_2 = 0, n = 2) \\
&\times \; D_{cwff}(w, 360°, \psi_2, \theta_0, \theta_2 = 0, n = 2)]\} \qquad (3)
\end{aligned}
$$

The third-order diffracted field consists of eight scattering mechanisms. The four emanating from the right side of the plate are demonstrated in Fig. 4. Four analogous mechanisms exist for the left side of the plate. The total third-order diffracted field is:

$$
\begin{aligned}
\mathbf{E_{3rd}} \;=\; & \mathbf{E_i} \frac{e^{-jk\rho}}{\sqrt{k\rho}} \frac{e^{-j2kw}\sqrt{k}}{4w} \left\{ e^{-j\frac{kw}{2}(\cos\phi' + \cos\phi)} \right. \\
&\times \; [D_{pwfd}(w, \psi_1', 0°, \theta_0, \theta_2 = 0, n = 2) \\
&\times \; D_{cwff}(w, 0°, \psi_1, \theta_0, \theta_2 = 0, n = 2)
\end{aligned}
$$

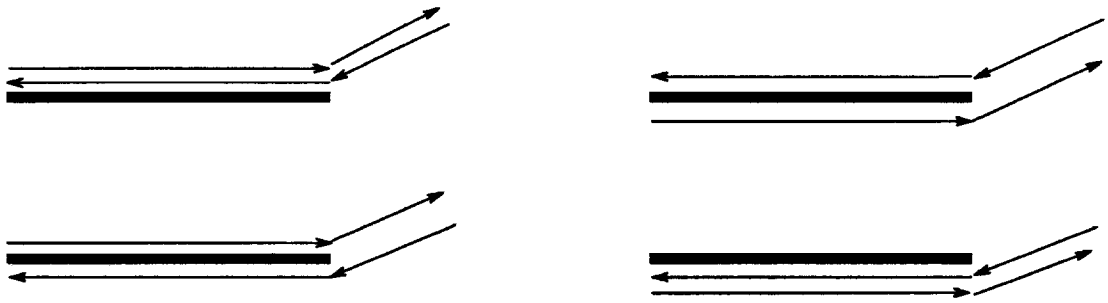

Figure 4: Third-order scattering terms emanating from the right edge of the plate.

$$
\begin{aligned}
&\times \; D_{cwff}(\frac{w}{2}, 0°, 0°, \theta_0, \theta_2, n = 2) \\
&+ \; D_{pwfd}(w, \psi_1', 360°, \theta_0, \theta_2 = 0, n = 2) \\
&\times \; D_{cwff}(w, 360°, \psi_1, \theta_0, \theta_2 = 0, n = 2) \\
&\times \; D_{cwff}(\frac{w}{2}, 360°, 360°, \theta_0, \theta_2, n = 2) \\
&+ \; D_{pwfd}(w, \psi_1', 0°, \theta_0, \theta_2 = 0, n = 2) \\
&\times \; D_{cwff}(w, 360°, \psi_1, \theta_0, \theta_2 = 0, n = 2) \\
&\times \; D_{cwff}(\frac{w}{2}, 0°, 360°, \theta_0, \theta_2, n = 2) \\
&+ \; D_{pwfd}(w, \psi_1', 360°, \theta_0, \theta_2 = 0, n = 2) \\
&\times \; D_{cwff}(w, 0°, \psi_1, \theta_0, \theta_2 = 0, n = 2) \\
&\times \; D_{cwff}(\frac{w}{2}, 360°, 0°, \theta_0, \theta_2, n = 2)\Big] \\
&+ \; e^{j\frac{kw}{2}(\cos\phi' + \cos\phi)} \\
&\times \; [D_{pwfd}(w, \psi_2', 0°, \theta_0, \theta_2 = 0, n = 2) \\
&\times \; D_{cwff}(w, 0°, \psi_2, \theta_0, \theta_2 = 0, n = 2) \\
&\times \; D_{cwff}(\frac{w}{2}, 0°, 0°, \theta_0, \theta_2, n = 2)
\end{aligned}
$$

$$
\begin{aligned}
&+ \; D_{pwfd}(w, \psi_2', 360°, \theta_0, \theta_2 = 0, n = 2) \\
&\times \; D_{cwff}(w, 360°, \psi_2, \theta_0, \theta_2 = 0, n = 2) \\
&\times \; D_{cwff}(\frac{w}{2}, 360°, 360°, \theta_0, \theta_2, n = 2) \\
&+ \; D_{pwfd}(w, \psi_2', 0°, \theta_0, \theta_2 = 0, n = 2) \\
&\times \; D_{cwff}(w, 360°, \psi_2, \theta_0, \theta_2 = 0, n = 2) \\
&\times \; D_{cwff}(\frac{w}{2}, 0°, 360°, \theta_0, \theta_2, n = 2) \\
&+ \; D_{pwfd}(w, \psi_2', 360°, \theta_0, \theta_2 = 0, n = 2) \\
&\times \; D_{cwff}(w, 0°, \psi_2, \theta_0, \theta_2 = 0, n = 2) \\
&\times \; D_{cwff}(\frac{w}{2}, 360°, 0°, \theta_0, \theta_2, n = 2)\Big]\Big\} \qquad (4)
\end{aligned}
$$

In the above equation, $\frac{w}{2}$ is used at some points as the distance parameter because the diffraction coefficient at these points is for cylindrical-wave incidence from a distance of w and observation at a finite distance of w. For this case, a distance parameter of $\frac{\rho'\rho}{\rho'+\rho} = \frac{w}{2}$ must be used. Another point of greater importance is that the UTD diffraction coefficients for the impedance wedge developed in [13] are identically zero for grazing incidence, which is the angle of incidence necessary for incorporating higher-order diffraction terms. Tiberio, *et al.*, performed a more precise expansion of Maluizhinets' solution to the impedance wedge problem and, thus, developed an appropriate diffraction coefficient for the case of grazing incidence (see [13] Eq. (16)). The incorporation of this coefficient into our model is a future goal of this research. For the results generated in this report, the value of the diffraction coefficient for grazing incidence is calculated $\frac{1}{100}th$ of a degree from grazing using the ordinary UTD coefficients of Eq. (4) in [8]. The results using this approximation are quite good, as will be demonstrated in the results section of this report. It is expected that incorporating the more precise coefficient of Eq. (16) in [13] will achieve even better results.

Surface wave fields exist only for certain angular regions and surface impedances given by Eqs. (17) and (18) in [8]. Surface wave transition fields compensate for discontinuities in the surface wave field at the surface wave shadow boundaries in a manner analogous to the way in which diffracted fields compensate for discontinuities in the geometrical optics field at the incident and reflection shadow boundaries. The surface wave transition fields also add to the total field everywhere, as do the diffracted fields.

The model of this report includes second- and third-order diffracted surface wave and surface-wave transition fields. The expressions for the total fields are cumbersome and similar in form to Eqs. (3) and (4) above, so they will not be included here. The general expression for the total nth-order diffracted field, including the surface wave and surface wave transition terms is:

$$\begin{aligned} \mathbf{U}_{nth} &= \mathbf{U}_i \prod_{i=1}^{n-1} \left[D(\psi_i', \psi_i, \rho_i) \frac{e^{-jk\rho_i}}{\sqrt{\rho_i}} + U_{sw_i} + U_{swtr_i} \right] \\ &\times D(\psi_n', \psi_n, \rho_n) \frac{e^{-jk\rho}}{\sqrt{\rho}} \end{aligned} \tag{5}$$

2. Contributions of Higher-Order Scattering Mechanisms

Although a model that includes first-order diffractions is accurate near and at normal incidence to the plate, it is an insufficient model for accurately predicting the scattering at all angles. For angles away from normal incidence, higher-order diffraction terms and surface wave terms are crucial. A breakdown of the contributions of the various terms is shown in Figs. 5 - 8 for a 2λ by 2λ plate coated on one side with a coating of thickness $t = 0.04121\lambda$ and with material parameters $\mu_c = 1.539 - j1.2241$ and $\epsilon_c = 11.826 - j0.16639$. The results are shown for a frequency of 10 GHz. In all the figures, the solid black line represents the total field calculated using the UTD model. This model includes first-, second-, and third-order regular diffractions, and second- and third-order surface wave and surface wave transition terms.

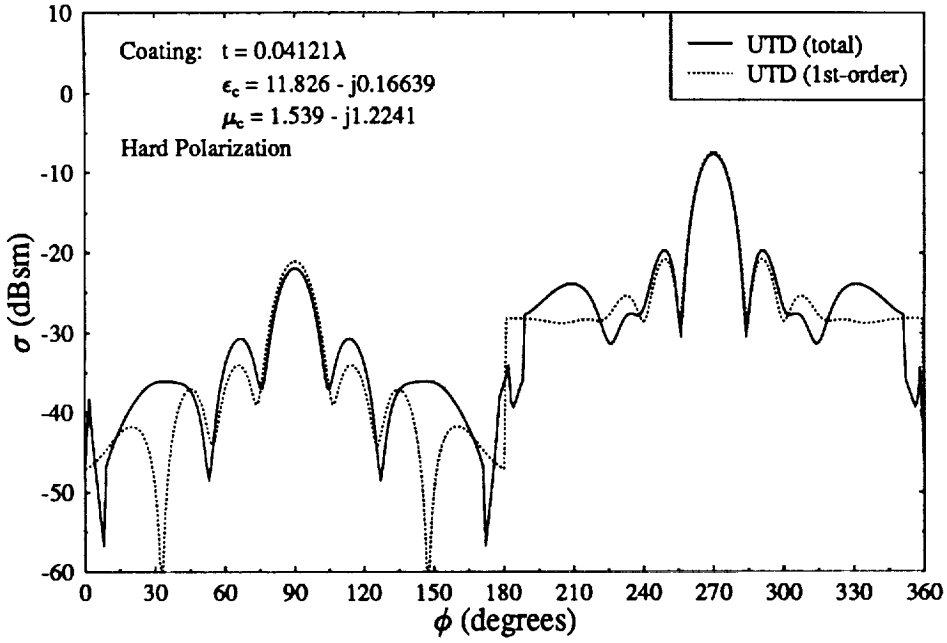

Figure 5: Breakdown of the UTD components ($w = L = 2.0\lambda$, $f = 10.0$ GHz).

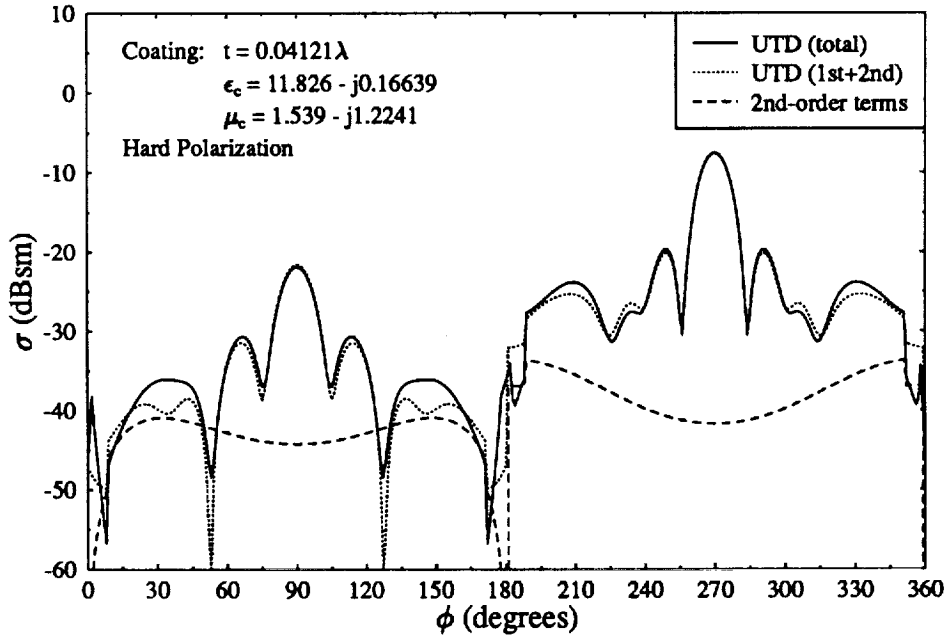

Figure 6: Breakdown of the UTD components ($w = L = 2.0\lambda$, $f = 10.0$ GHz).

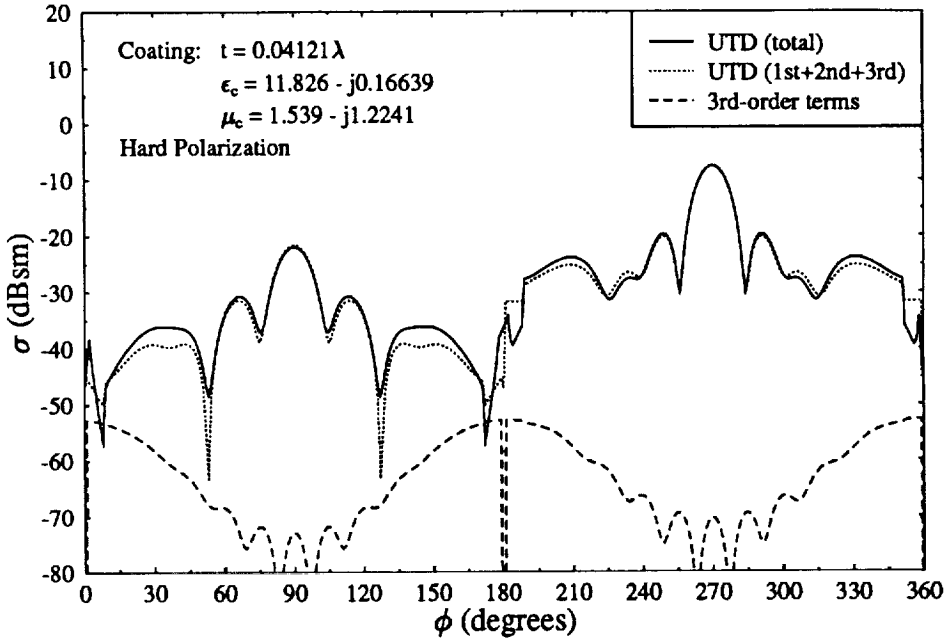

Figure 7: Breakdown of the UTD components ($w = L = 2.0\lambda$, $f = 10.0$ GHz).

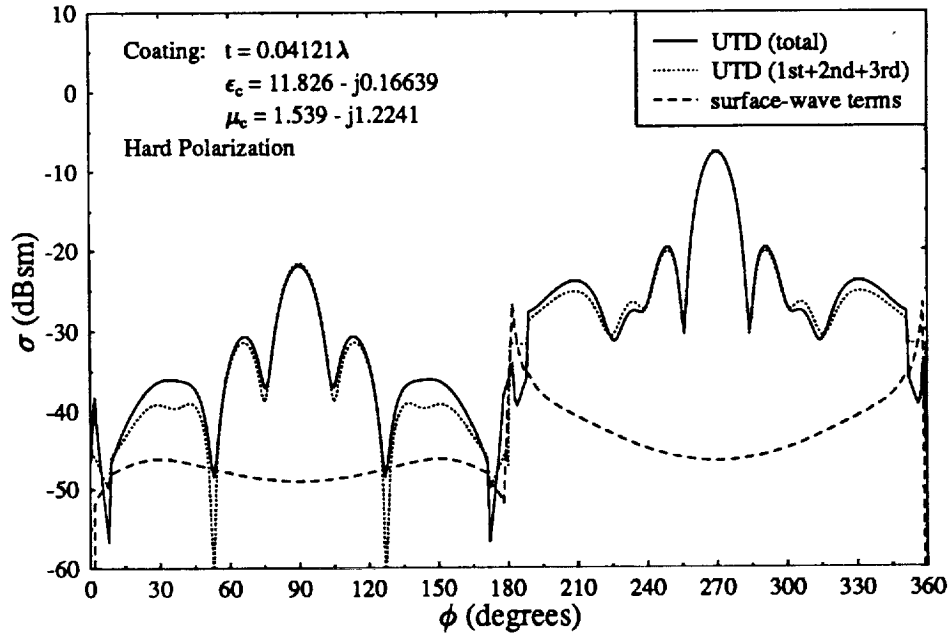

Figure 8: Breakdown of the UTD components ($w = L = 2.0\lambda$, $f = 10.0$ GHz).

Fig. 5 compares the total UTD field to the field calculated using only first-order diffractions. Near and at normal incidence to both sides of the plate, the two models agree fairly well indicating that first-order diffractions are the main contributing mechanisms at these angles. Away from the main lobe, however, it is apparent that higher-order terms are major contributors to the scattered field. The two models differ drastically in the region extending from grazing incidence to approximately 60° away from grazing on both sides of the plate.

Fig. 6 illustrates that second-order diffractions are the major higher-order contributing mechanisms. The dotted line in this figure is the UTD field calculated using only first- and second-order diffraction terms. The dashed line is the magnitude of the second-order diffractions only. For the main lobe on both sides of the plate, the second-order terms are not significant; however, away from this lobe, they become crucial. The first minor lobes are predicted fairly well with the addition of the second-order terms. In the grazing lobes, especially on the coated side of the plate, there is still a need for higher-order terms to complete the model.

The third-order diffraction terms improve the results in the grazing lobes somewhat, as illustrated in Fig. 7, where the dotted line represents a UTD model containing first-, second-, and third-order regular diffractions. The dashed line representing the magnitude of the third-order field indicates that these fields are very minor compared to the other fields. Fig. 8 illustrates that surface wave and surface wave transition fields are crucial to the overall RCS pattern in the grazing lobes. The solid line is the total field containing the surface wave and surface wave transition fields while the dotted line does not contain these terms. The difference between the two predicted fields is obvious in the lobes near grazing. As the dashed line representing the magnitude of the surface wave and surface wave transition fields indicates, the surface wave fields represent a larger contribution to the total field than the third-order fields.

3. Results

To validate the coated plate UTD model, measured RCS data was obtained for two different physical plates at several different frequencies using the ElectroMagnetic Anechoic Chamber (EMAC) at Arizona State University (ASU). The two plates, which will be referred to as Plate A and Plate B, are characterized by the following parameters:

- Plate A
  - size: 6.0 cm $\times$ 6.0 cm
  - plate material: Aluminum (25.0 mils)
  - coating material: SWAM (commercially available ferrite-loaded RAM)
  - coating thickness: 48.642 mils
  - relative permittivity of coating: $\epsilon_c = 11.826 - j0.16639$
  - relative permeability of coating: $\mu_c = 1.539 - j1.2241$
  - frequency of measurement: 10.0 GHz
  - plate size in wavelengths: $2.0\lambda \times 2.0\lambda$
  - coating thickness in wavelengths: 0.04121λ
- Plate B
  - size: 3.1625 in. $\times$ 3.1625 in.
  - plate material: Brass (10.0 - 15.0 mils)
  - coating material: GDS (commercially available ferrite-loaded RAM)
  - coating thickness: 33.177 mils
  - relative permittivity of coating: $\epsilon_c = 13.927 - j0.208$
  - relative permeability of coating: $\mu_c = 1.446 - j1.140$
  - frequencies of measurement: 9.4842 GHz, 11.1964 GHz, and 12.053 GHz
  - plate sizes in wavelengths: $2.54\lambda \times 2.54\lambda$, $3.0\lambda \times 3.0\lambda$, and $3.23\lambda \times 3.23\lambda$
  - coating thicknesses in wavelengths: 0.0267λ, 0.03147λ, 0.03388λ

Plate A is electrically smaller than Plate B, and Plate A has a lossier coating than Plate B. For these reasons, the UTD model is less accurate for Plate A than it is for Plate B. The data indicates that the UTD model improves in accuracy as the electrical size of the plate increases and as the coating becomes electrically thinner

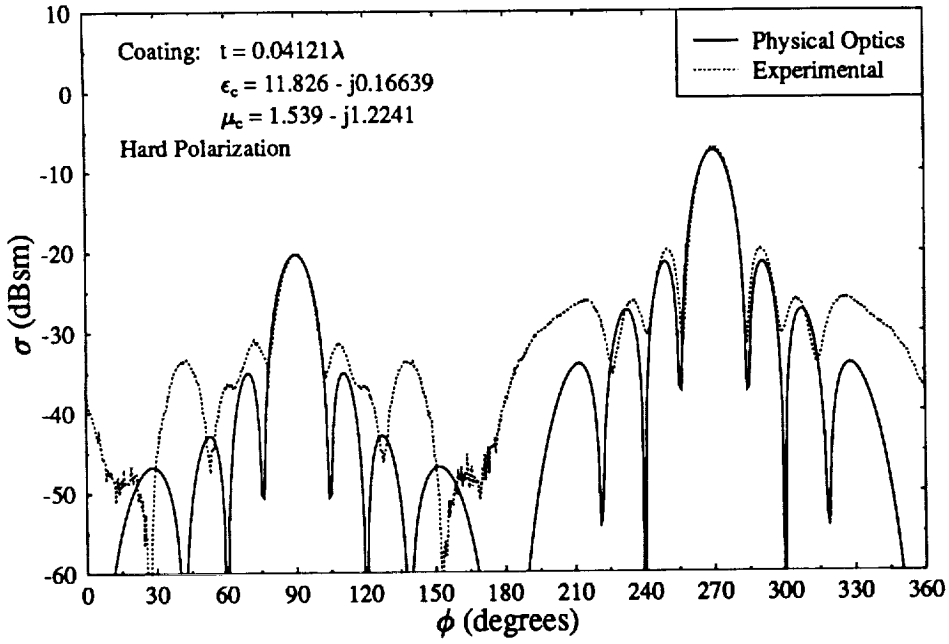

Figure 9: Monostatic RCS of Plate A ($w = L = 2.0\lambda$, $f = 10.0$ GHz).

and less lossy. The data presented in the next few figures demonstrates that the UTD model, which accounts for edge effects, is much more accurate than the PO model, which does not include the effects of interacting edges.

Fig. 9 contains graphs of the PO and experimental data for Plate A. Although there is excellent agreement in the main lobe, the PO model becomes increasingly inaccurate away from the main lobe, especially on the coated side of the plate ($0° < \phi < 180°$). Fig. 10 demonstrates that the UTD model is much more accurate. On the perfectly conducting side of the plate, the UTD model agrees fairly well in the main lobe and first two side lobes. On the coated side of the plate, there is much inaccuracy; however, the results are still better than those obtained using the PO model. The two biggest areas of concern are the discontinuities apparent at the grazing angles near $\phi = 180°$ and the discrepancy at normal incidence to the coated side of the plate. These areas are being investigated.

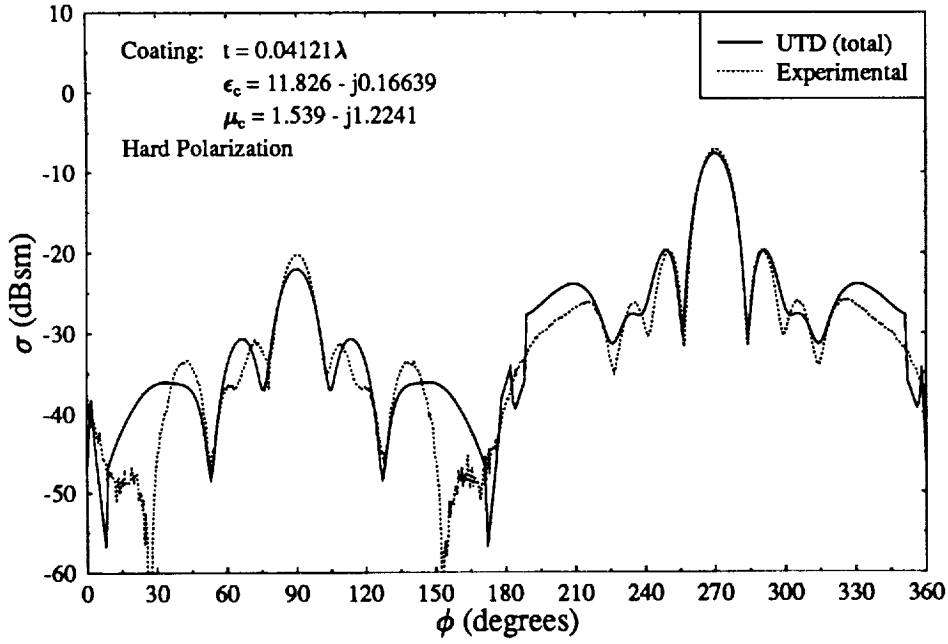

Figure 10: Monostatic RCS of Plate A ($w = L = 2.0\lambda$, $f = 10.0$ GHz).

The results for Plate B demonstrate that the UTD model becomes much more accurate as the electrical size of the plate increases. Fig. 11 contains PO and experimental data for Plate B at 9.5 GHz. Agreement between the two sets of data is excellent for the main lobe and first side lobe on both sides of the plate; however, the agreement between the UTD data and the experimental results, shown in Fig. 12, shows much better agreement. On both sides of the plate, agreement is almost exact in the main lobe and first two side lobes. Agreement even in the grazing lobes is very good. At higher operational frequencies, the agreement between the UTD model and experiment remains consistently good. Figs. 13 and 14 show the results for Plate B at 11.2 GHz, and Figs. 15 and 16 show the results for 12.1 GHz.

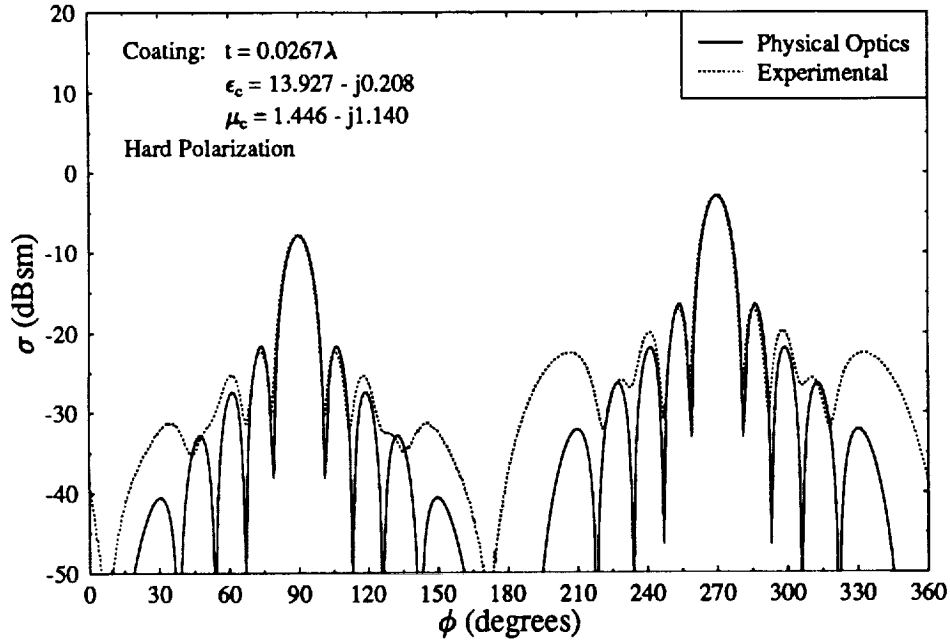

Figure 11: Monostatic RCS of Plate B ($w = L = 2.54\lambda$, $f = 9.5$ GHz).

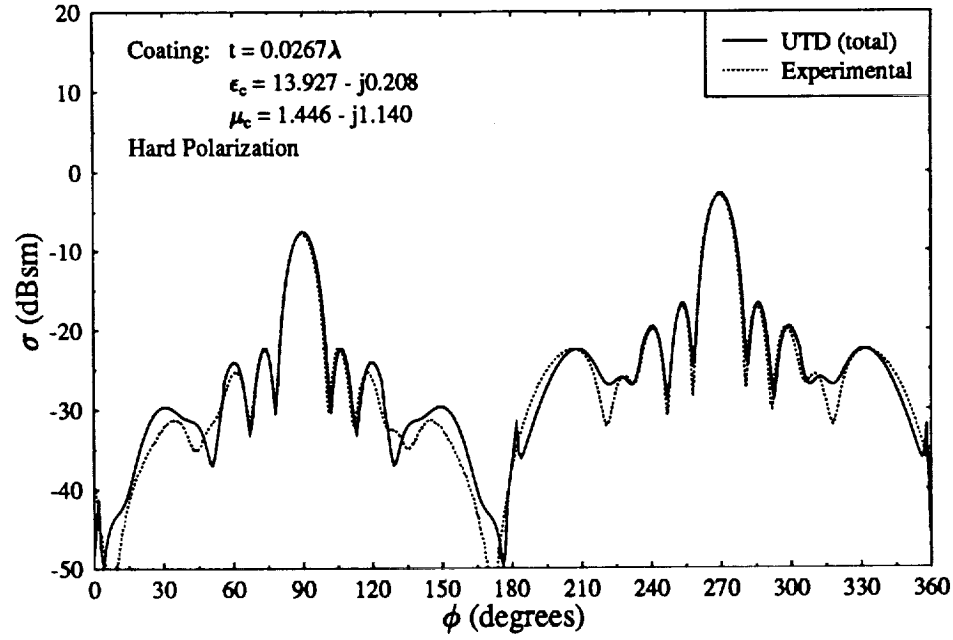

Figure 12: Monostatic RCS of Plate B ($w = L = 2.54\lambda$, $f = 9.5$ GHz).

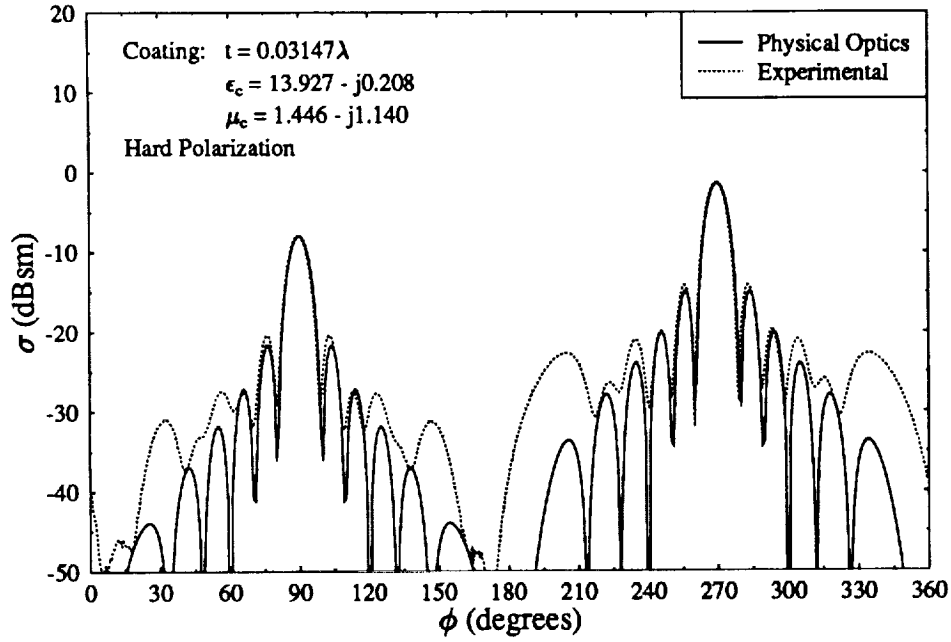

Figure 13: Monostatic RCS of Plate B ($w = L = 3.0\lambda$, $f = 11.2$ GHz).

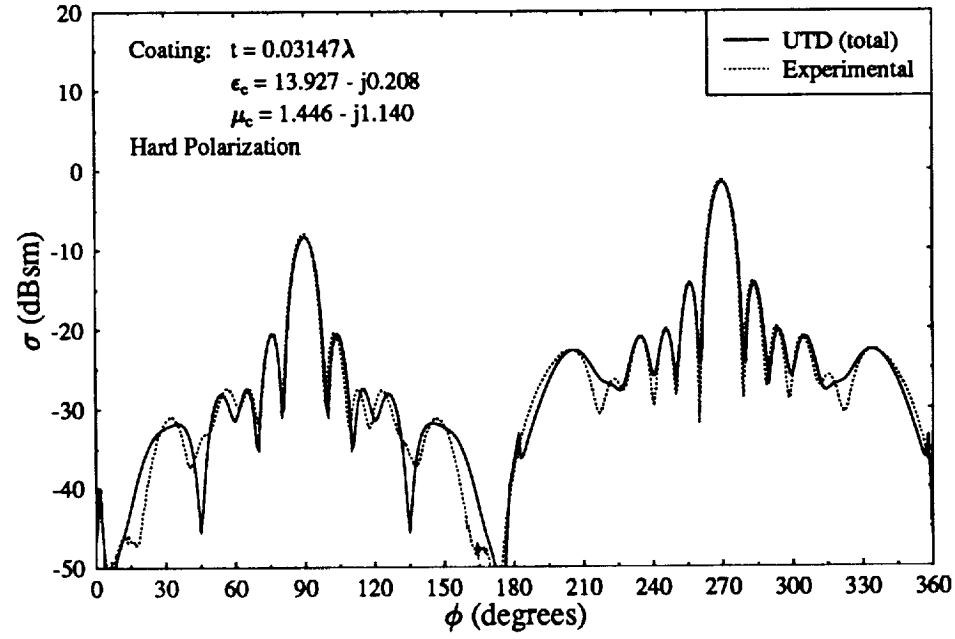

Figure 14: Monostatic RCS of Plate B ($w = L = 3.0\lambda$, $f = 10.0$ GHz).

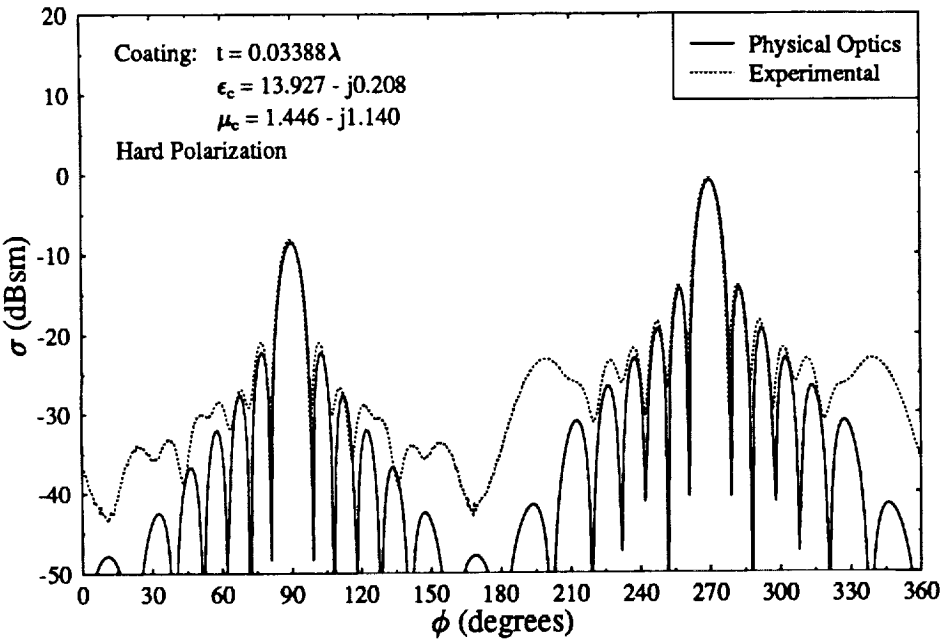

Figure 15: Monostatic RCS of Plate B ($w = L = 3.23\lambda$, $f = 12.1$ GHz).

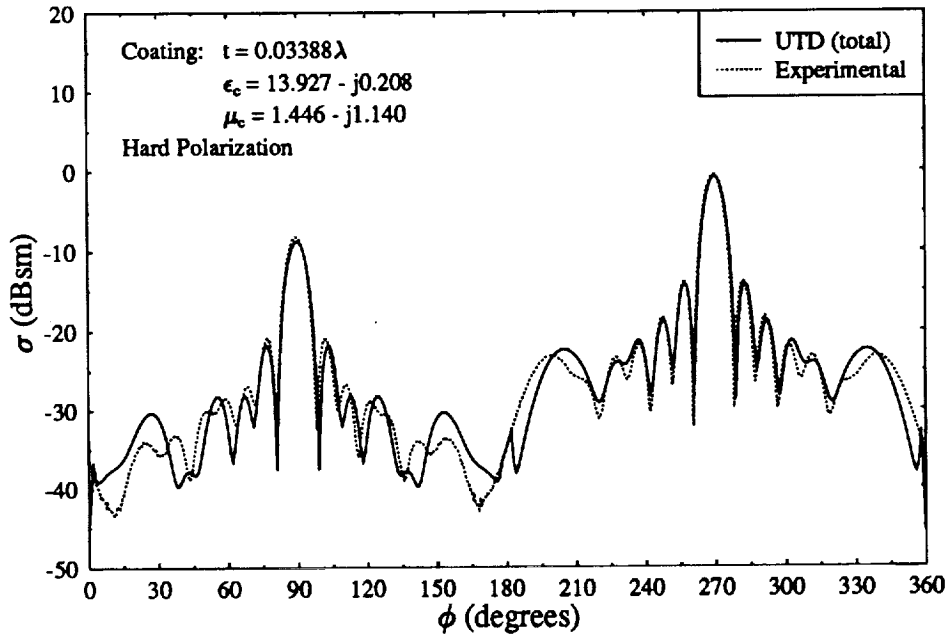

Figure 16: Monostatic RCS of Plate B ($w = L = 3.23\lambda$, $f = 12.1$ GHz).

C. FUTURE WORK

We have demonstrated a fairly accurate, yet computationally simple and fast, UTD model for coated plate scattering in the principal plane. Immediate future work will address modifications and refinements of this model. Particularly, the more accurate UTD diffraction coefficients formulated by Tiberio, *et al.* [13], will be used for modeling higher-order diffractions. This should result in better accuracy. Also, the use of the ESRM of Herman and Volakis [15] will be investigated to see if more accurate results can be obtained using this method.

The ultimate goal of this research is to be able to apply the UTD for coated wedges to general geometries. In order to realize this goal, the method must remain general. Other areas of possible future research include the use of the ESRM and of higher-order generalized impedance boundary conditions (GIBC's); however, the drawback of these techniques is that they are specific to a geometry and must often be reformulated for each target of interest. Also, although the area of GIBC's is promising, current research indicates that using GIBC's often results in non-unique solutions [21]. Despite these drawbacks, future research will look at the possibility of including the ESRM and GIBC's in a UTD model. Other future goals include extending the principal-plane plate model to nonprincipal planes by incorporating equivalent currents techniques. Also, the UTD for coated wedges will be applied to the dihedral corner reflector.